

# Flexible Lithium-Ion Conducting Composite Electrolyte

Brent Conway,<sup>[a]</sup> Katherine Jewell,<sup>[b]</sup> and Cameron Tanner<sup>\*[a]</sup>

Incorporation of a solid electrolyte into lithium-ion batteries brings with it the potential to increase energy density, improve operational lifetime, and enhance safety. Although numerous ceramics with high lithium-ion conductivity have been identified, use in batteries is hindered by fragility, inefficiency of fabrication processes, and difficulty sintering to a hermetic state. We present a novel composite electrolyte with nearly single crystal grains of  $\text{Li}_{1.3}\text{Al}_{0.3}\text{Ti}_{1.7}(\text{PO}_4)_3$  embedded within a

flexible, PDMS polymer matrix. Each lithium-ion conducting particle is exposed on both sides of the membrane to provide a fast conduction pathway that is unimpeded by grain boundaries. Membranes made with this structure and grains grown by slow cooling from the melt are hermetic and have lithium conductivity of  $\sim 2.7 \times 10^{-4} \text{ S cm}^{-1}$ . The principal conductivities of  $\text{Li}_{1.3}\text{Al}_{0.3}\text{Ti}_{1.7}(\text{PO}_4)_3$  crystals are  $\sigma_a = 3.4 \times 10^{-3}$  and  $\sigma_c = 1.1 \times 10^{-3} \text{ S cm}^{-1}$ .

## 1. Introduction

Ion conducting ceramics are proposed for use as the electrolyte in a wide variety of technological applications such as energy conversion, energy storage, and sensing.<sup>[1]</sup> Several attributes of solid electrolytes make them attractive. Thermodynamic stability eliminates flammability as a safety concern. The ionic transport mechanism of a ceramic is especially selective so secondary reactions that could occur with other types of electrolytes are inhibited. A solid does not evaporate so there is no need to manage its state of hydration to prevent either drying or flooding conditions.<sup>[2]</sup> Poisoning and short-circuiting that result from dendrite formation are also inhibited as the solid membrane blocks transfer of material and prevents contact between anode and cathode regions.<sup>[3]</sup> A solid electrolyte is not mobile so the electrode-electrolyte interface is defined by placement of the components rather than flow of a liquid.

Despite these attractive features, real-world applications of ceramic electrolytes are limited. Cardiac pacemaker batteries developed in the 1970's employ a lithium iodide/alumina solid electrolyte<sup>[4]</sup>. Sodium sulfur batteries that employ a sodium  $\beta$ -alumina electrolyte are used in grid support and renewable energy storage systems.<sup>[5]</sup> Yttria-stabilized zirconia is extensively used as an oxygen or lambda sensor in a wide variety of applications ranging from steelmaking<sup>[6]</sup> to engine control in automobiles<sup>[7]</sup>. There are many other potential applications

under development. Solid oxide fuels have been the subject of commercial development for more than 40 years. The most commonly utilized electrolyte material is 8 mole percent yttria-stabilized zirconia<sup>[8]</sup> with other materials such as doped ceria<sup>[9]</sup> or lanthanum gallate also receiving attention.<sup>[10]</sup> There is a tremendous opportunity for solid electrolytes in lithium-ion batteries for construction of safer, all solid-state cells and to enable higher capacity sulfur cathodes.<sup>[11]</sup>  $\text{Li}_{1+x}\text{Al}_x\text{Ti}_{2-x}(\text{PO}_4)_3$  (LATP),<sup>[12]</sup>  $\text{Li}_x\text{La}_{(2-x)/3}\text{TiO}_3$  (LLT),<sup>[13]</sup> and most recently stuffed garnets<sup>[14]</sup> are favored material systems.

Three principle barriers have hindered wider use of solid electrolytes. The ionic conductivity of polycrystalline ceramics is often below a threshold of  $10^{-4} \text{ S cm}^{-1}$  needed to deliver a useful level of power.<sup>[15]</sup> One solution to the low ionic conductivity is to make the electrolyte as thin as possible. However, ceramic materials are brittle and have low strain tolerance. The likelihood of breakage during fabrication or when in use in a device is exacerbated when the electrolyte is thin.<sup>[16]</sup> Traditional ceramic forming and sintering processes are challenged to deliver a product with tight control over dimensions and that is hermetic.<sup>[17]</sup> Sintering of lithium and sodium containing electrolytes is further complicated by the high volatility of the alkaline oxides at temperatures above about 1000 °C.<sup>[18]</sup>

In this work, we demonstrate a novel, monograin composite structure that addresses these barriers in applications where use temperatures are below about 200 °C. The structure is shown in Figure 1 and consists of ionically conductive particles of ceramic that span the full thickness of a continuous polymer matrix.<sup>[19]</sup> The monograin structure differs from other polymer-ceramic electrolytes<sup>[20]</sup> in that the same particle is exposed on both sides of the membrane rather than being fully enveloped by the polymer. The continuous polymer matrix phase imparts toughness, high strain tolerance, and flexibility to make handling easier and enhance durability. The structure can be made using efficient polymer processing techniques and avoids expensive, high temperature ceramic forming and processing steps. This monograin structure also enables increased ionic conductivity. Grain boundaries in polycrystalline ceramics like

[a] B. Conway, Dr. C. Tanner  
Department of Crystalline Materials Research  
Corning Incorporated  
SP-DX-02-C, Corning, New York, 14831, U.S.A  
E-mail: tannercw@corning.com

[b] K. Jewell  
Department of Organic Technologies  
Corning Incorporated  
SP-AR-01-1, Corning, New York, 14831, U.S.A

 Supporting information for this article is available on the WWW under  
<https://doi.org/10.1002/batt.201900212>

 An invited contribution to a Special Collection on Electrolytes for Electrochemical Energy Storage

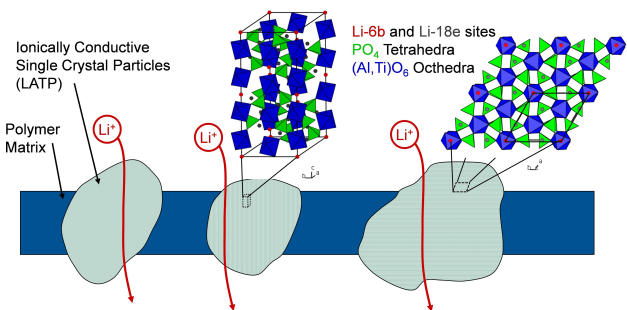


**Figure 1.** Illustration of a composite electrolyte with monograins of LATP embedded within a polymer film. The monograins span the thickness of the polymer for low impedance pathways for lithium-ion transport.

LATP, LLT, and sodium  $\beta$ -alumina severely impede flow of ions. Lithium-ion conductivity within a crystal of sintered LATP, as an example, is 50 to 100 times greater than realized in the polycrystalline state.<sup>[21]</sup> The composite structure confers single crystal conductivity to the membrane level as a result of embedded grains that are monocrystalline or nearly so. Structures like the monograin composite electrolyte are described for flexible photoconductors based upon CdS.<sup>[22]</sup>

## 2. Results and Discussion

The LATP compositional family was selected for investigation of the monograin composite electrolyte concept. Members of this family have lattice ion conductivity greater than  $10^{-3} \text{ S cm}^{-1}$  and ionic transport numbers that are nearly one. Two methods to grow large monograins were explored: extended sintering to provide time for grain growth and slow cooling from the melt to favor growth over nucleation. Both approaches give materials suitable for monograin composite electrolytes.

Sintering of  $\text{Li}_{1.3}\text{Al}_{0.3}\text{Ti}_{1.7}(\text{PO}_4)_3$  between 1050 and 1200 °C for times of 24 to 240 hr provided conditions for grains to ripen and reach sizes in excess of 50  $\mu\text{m}$ , see Figure 2a. The prospects for growth of LATP from a melt were uncertain due to limited information about phase equilibria in the  $\text{Li}_2\text{O}-\text{TiO}_2-\text{P}_2\text{O}_5$  system and  $\text{LiTi}_2(\text{PO}_4)_3$  (LTP). Melts of  $\text{Li}_{1+x}\text{Al}_x\text{Ti}_{2-x}(\text{PO}_4)_3$  with  $x=0.15, 0.3$ , and 0.4 made at 1500 °C were clear and contained no sediment. Cooling of the melts at  $10^\circ\text{C hr}^{-1}$  to 1000 °C gave grains larger than 500  $\mu\text{m}$  in size. An image of the surface of the melt with visible faceting as an indicator of the large grain size is shown in Figure S1. Powder x-ray diffraction (XRD) confirmed that the dominant phase for materials made by both methods has the LTP structure with an amount that can exceed 90% on the basis of diffraction peak intensity, see Figure 2b. Minor phases of rutile and  $\text{AlPO}_4$  are also present with amounts per condition detailed in Table S2. For sintering, concentrations of minor phases grow as time and temperature are increased due to lithium volatilization. In comparison, the amounts of rutile and  $\text{AlPO}_4$  from the melt increase with the doping level, “ $x$ ” as can be seen in XRD traces in Figure 2b. The composition of the LATP that crystallizes from the melt evolves during cooling due to temperature dependency of the solidus. The

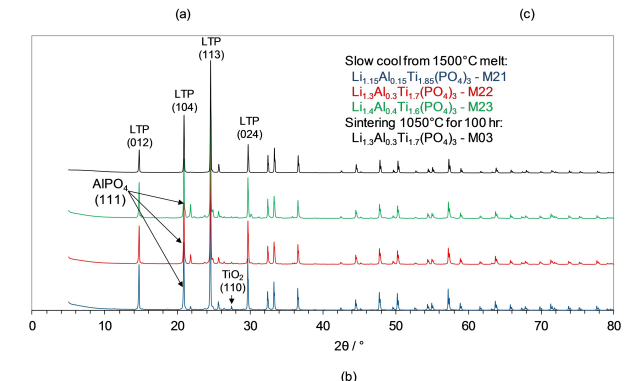
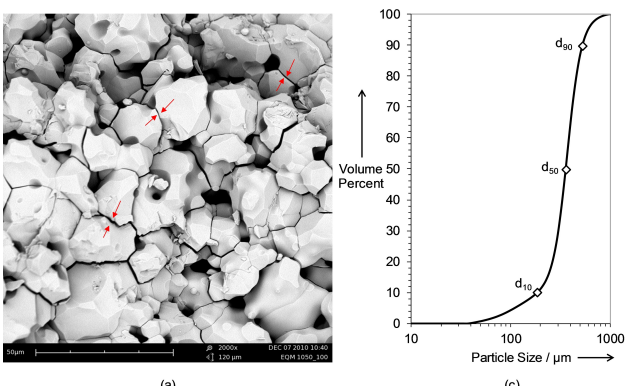


**Figure 2.** a) SEM image of a fracture surface of  $\text{Li}_{1.3}\text{Al}_{0.3}\text{Ti}_{1.7}(\text{PO}_4)_3$  (C2) sintered for 100 hr at 1050 °C with red arrows highlighting microcracks, b) powder XRD traces for selected LATP compositions and processes, and c) the cumulative particle size distribution after manual grinding.

solidus composition rather than that of the original melt dictates composition of the LATP. Compositional zoning and inhomogeneity are visible in SEM images of polished cross-section shown in Figure S2.

The size of the grains is so large that traditional grinding and classification processes can generate powders with a size ideal for a composite electrolyte, 20–200  $\mu\text{m}$ , in which most of the particles are monograins. In the case of LATP, large grains with an inherently narrow particle size distribution were generated with mild, manual grinding. The crystal structure of LATP is hexagonal and belongs to the R-3c space group. It consists of corner sharing tetrahedra of  $\text{PO}_4$  and octahedra of  $(\text{Al},\text{Ti})\text{O}_6$ . Units of  $[(\text{Al},\text{Ti})_2(\text{PO}_4)_3]$  are linked in chains that run parallel to the c-axis.  $\text{Li}^+$  are distributed over 6b and the numerous and mostly vacant 18e sites that are between the polyhedra. The structure provides an open network for  $\text{Li}^+$  conduction. The bonding arrangement is also responsible for a dramatic anisotropy in lattice thermal expansion. The coefficients of lattice thermal expansion between 20 and 800 °C in the a and c-directions of LTP are  $0.6 \times 10^{-6}$  and  $30.9 \times 10^{-6} \text{ }^\circ\text{C}^{-1}$ .<sup>[23]</sup> The difference in lattice expansions in the two directions leads to build up elastic strain energy between grains of different orientations upon cooling from sintering or after solidification of the melt. The elastic strain energy is released by formation of microcracks when a critical grain size is exceeded. The critical grain size is estimated to be about 5  $\mu\text{m}$  for LTP and much smaller than the materials produced here.<sup>[24]</sup>

The microcracks in  $\text{Li}_{1.3}\text{Al}_{0.3}\text{Ti}_{1.7}(\text{PO}_4)_3$  sintered for 100 hr at 1050°C are evident in the SEM micrograph of a fracture surface shown in Figure 2a. The microcracks are primarily intergranular and so monograins that have a size distribution closely related to the original material are formed. A narrow size distribution for the monograins is preferred to maximize the number of particles that can be exposed on both sides of the membrane and to limit surface roughness. The cumulative size distribution from laser scattering is shown in Figure 2c for the aforementioned material after manual crushing. It has a breadth factor,  $(d_{90}-d_{10})/d_{50}$ , where "d" is the particle size corresponding the cumulative percentile indicated by the subscript. The breadth factor is about one; sufficiently narrow for preparation of a monograin composite electrolyte. The particle size distribution could be further narrowed by sieving or air-classification.

Flexible, functional, and hermetic composite electrolyte membranes were prepared by spin coating and chemical etching. One membrane is shown in Figure 3a and 3b. The membrane consists of monograins of  $\text{Li}_{1.3}\text{Al}_{0.3}\text{Ti}_{1.7}(\text{PO}_4)_3$  obtained by slow cooling from the melt that were ground and sieved to give particle sizes ranging from between 250 and 355  $\mu\text{m}$ . The monograins were mixed with polydimethylsiloxane (PDMS) solution, Dow Corning Sylgard 184, in a 1:4 weight ratio and spin coated at 500 rpm for 10 seconds onto a glass surface. Residual PDMS coating the surfaces of the

monograins was removed by etching with a solution of *N*-methylpyrrolidone and tetra-*n*-butylammonium fluoride. An etching time of 15 min was found to be near an optimum. Etching times that are too short do not fully remove the silicone to expose the monograins, and etching for longer times breaks the membrane. The thickness of the silicone in the finished membrane is 140  $\mu\text{m}$ . Even smaller, ~250  $\mu\text{m}$  monograins will straddle and protrude from the polymer matrix to provide pathway uninterrupted by grain boundaries across the composite electrolyte. The translucent, and in some cases transparent, appearance of the monograins is an indication that they are single or nearly single crystal in character and free of grain boundaries that interfere with lithium-ion conduction.

Lithium-ion conductivity was determined by impedance spectroscopy using a Solartron 1287 Electrochemical Interface with a 1260 Frequency Response Analyzer on samples with an active area of 72.4  $\text{mm}^2$  that were coated by PVD with gold blocking electrodes. A Cole-Cole plot of imaginary vs. real resistances collected at frequencies between 1 Hz and 1 MHz is presented in Figure 3c. The effectiveness of the monograin structure in reducing grain boundary impedance is evident. The semicircle in the Cole-Cole plot that is characteristic of grain boundary resistance in polycrystalline lithium-ion conductors is absent in the composite electrolyte.<sup>[21]</sup> The DC resistance of the composite electrolyte was taken as the high frequency intercept of the curve with the real axis, ~175  $\Omega$ . After accounting for geometric factors, the lithium-ion conductivity of the membrane was  $2.7 \times 10^{-4} \text{ Scm}^{-1}$ .

The principal conductivities of LATP were determined working with a few manually selected particles that were especially large in size,  $> 1 \text{ mm}$ . Candidate particles were embedded in epoxy, and the faces were polished flat and parallel. The surfaces were viewed under a scanning electron microscope and mapped by electron back scatter diffraction (EBSD). The EBSD map of orientation was used to determine if the particle was in fact a monograin. Images of three monograin particles of  $\text{Li}_{1.3}\text{Al}_{0.3}\text{Ti}_{1.7}(\text{PO}_4)_3$  sintered at 1150°C for 100 hr are shown in the mounts in Figure S3. Minor phases of  $\text{TiO}_2$ ,  $\text{AlPO}_4$ , and some  $\text{Al}_2\text{O}_3$  along with some trapped porosity were observed as shown in Figure 4. The inclusions do not strongly influence ion conduction as they are low in concentration and discontinuous. There is no sign of a grain boundary impedance in Cole-Cole plots shown in Figure 5a. However, the structure of particles obtained from slow cooling from the melt was more complex. The compositional zoning and arrangement of minor phases affected lithium-ion conduction. There are distinctive semicircles in the Cole-Cole plots that are indicative of interfacial resistances such as from phase boundaries.

Principal conductivities of  $\text{Li}_{1.3}\text{Al}_{0.3}\text{Ti}_{1.7}(\text{PO}_4)_3$  from a least-squares analysis of conductivity as a function of angle of tilt of the (0001) basal plane as defined by Eq. S1 are  $\sigma_a = 3.4 \times 10^{-3}$  and  $\sigma_c = 1.1 \times 10^{-3} \text{ Scm}^{-1}$ , see Figure 5. The conductivity in the basal plane is roughly a factor of 3 times greater than along the c-axis. The crystal structure of LATP is responsible for the large anisotropy and high  $\text{Li}^+$  conductivity in the basal plane. There are large channels with line of sight through the structure that connect 6b sites available for rapid migration of  $\text{Li}^+$ . In the c-

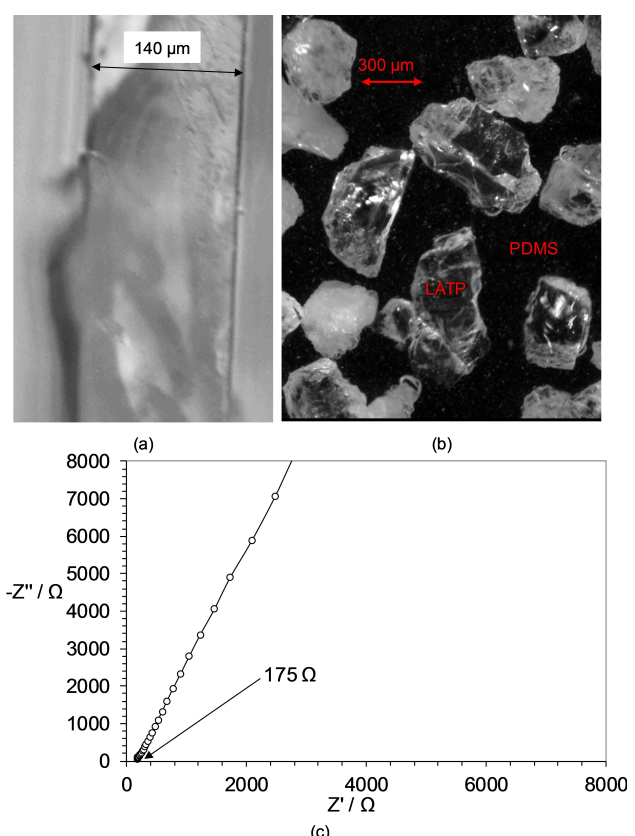


**Figure 3.** A spin-coated and etched composite electrolyte with monograins of  $\text{Li}_{1.3}\text{Al}_{0.3}\text{Ti}_{1.7}(\text{PO}_4)_3$  embedded in PDMS a) optical micrograph of cross section emphasizing the PDMS region, b) normal view of the monograins in the PDMS matrix, and c) Cole-Cole impedance plot.

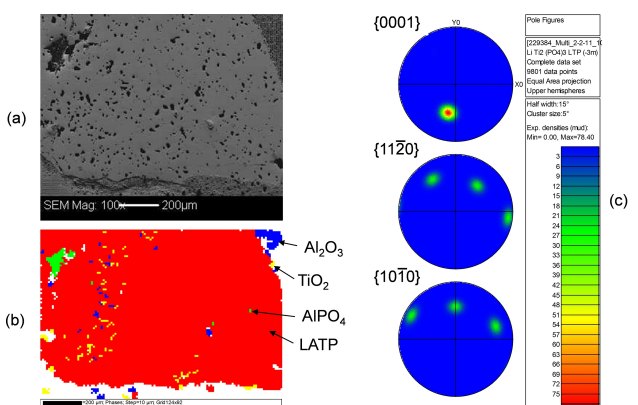


**Figure 4.** a) SEM image of a polished surface of an  $\text{Li}_{1.3}\text{Al}_{0.3}\text{Ti}_{1.7}(\text{PO}_4)_3$  particle obtained from extended sintering, b) map of phases from EBSD of the same region, and c) the pole figure showing the monograin character of the particle and its tilt.

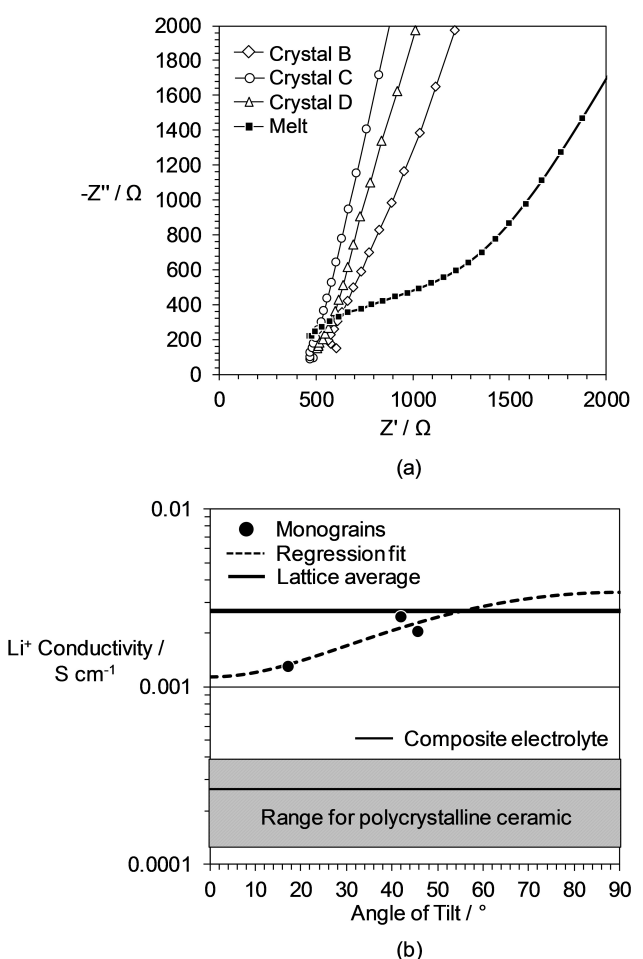


**Figure 5.** a) Cole-Cole plot of impedance data from monograins of  $\text{Li}_{1.3}\text{Al}_{0.3}\text{Ti}_{1.7}(\text{PO}_4)_3$  sintered at  $1150^\circ\text{C}$  for 100 hours and a particle of the same composition from slow cooling from the melt, and b)  $\text{Li}^+$  conductivity of monograins as a function of orientation with a regression fit to determine principal conductivities and comparison to  $\text{Li}^+$  conductivity of polycrystalline material of the same composition and the composite electrolyte described here.

direction,  $\text{Li}^+$  whether on 6b or 18e sites must traverse a slower, zig-zag path around  $\text{PO}_4$  tetrahedra and  $(\text{A}/\text{Ti})\text{O}_6$  octahedra.

The average conductivity for  $\text{Li}_{1.3}\text{Al}_{0.3}\text{Ti}_{1.7}(\text{PO}_4)_3$  monograins with random orientation and that is pertinent to the composite electrolyte is  $2.7 \times 10^{-3} \text{ S cm}^{-1}$ . The value is comparable to what has been reported in the literature for this composition.<sup>[12]</sup> It is also much greater than what was obtained with the composite electrolyte by a factor of ten. There are three factors that contribute to the disparity. First, the fractional surface area of the composite electrolyte occupied by ion conducting grains is about 40%, and the fraction of area exposed on the electrolyte faces will be reduced somewhat further due to geometry of the particles and how they intersect the surface of the matrix. These two effects are responsible for up to a four-fold reduction in average  $\text{Li}^+$  conductivity to  $6.8 \times 10^{-4} \text{ S cm}^{-1}$ . This same effect may be viewed from the perspective of the fabrication composite electrolyte. Second, the particles for the composite electrolyte were sourced from LATP grown by slow cooling from the melt. Particles from the melt process are not ideal for optimal conductivity in a composite electrolyte. Grain boundaries in some of the particles and compositional zoning reduce conductivity further. Third, the process for etching and removal of residual silicone from the surfaces of the grains is not fully optimized so some loss of active area or an additional source of impedance further reduce the conductivity. Each of these factors is directly controllable so a composite electrolyte with a  $\text{Li}^+$  conductivity of  $>10^{-3} \text{ S cm}^{-1}$  should be possible with process optimization.

### 3. Conclusions

We have demonstrated the concept of a flexible composite electrolyte based upon monograin particles of LATP. The membranes are hermetic and yield conductivity of greater than  $10^{-4} \text{ S cm}^{-1}$ . The concept is also able to scale much of the single crystal conductivity to the membrane level giving two important and related benefits. It provides higher conductivity and opens the door to compositions that have otherwise high grain boundary impedances. While the conductivity is sufficiently high, the thickness of the membrane would need to be reduced to 20–40  $\mu\text{m}$  to be used in batteries with high energy density. Lastly, the composite electrolyte concept is general and may be applied to other types of ion conductors such as sodium.

### Acknowledgements

We would like to thank Corning Incorporated for supporting this research.

### Conflict of Interest

The authors declare no conflict of interest.

**Keywords:** energy storage • ceramic • composite • electrolyte • lithium-ion batteries

- [1] K. Sundmacher, L. K. Rihko-Struckmann, *Galvita, Catal. Today* **2005**, *104*, 185–199.
- [2] W. Dai, H. J. Wang, X. Z. Yuan, J. J. Martin, D. J. Yang, J. L. Qiao, J. X. Ma, *Int. J. Hydrogen Energy* **2009**, *34*, 9461–9478.
- [3] a) S. Komaba, B. Kaplan, T. Ohtsuka, Y. Kataoka, N. Kumagai, H. Groult, *J. of Power Sources* **2003**, *119*–121, 378–382; b) J. Y. Song, Y. Y. Wang, C. C. Wan, *J. Power Sources* **1999**, *77*, 183–197.
- [4] D. Untereker in *Batteries for Implantable Biomedical Devices*, (Ed.: B. B. Owens), Plenum Press, New York, **1986**, pp. 51–81.
- [5] T. Oshima, M. Kajita, A. Okuno, *Int. J. App. Ceram. Tec.* **2004**, *1*, 269–276.
- [6] K. Yamada, Y. Shinya, *Solid State Ionics* **1981**, *3*–4, 595–598.
- [7] R. Ramamoorthy, P. K. Dutta, S. A. Akbar, *J. Mater. Sci.* **2003**, *38*, 4271–4282.
- [8] M. C. Martin, M. L. Mecartney, *Solid State Ionics* **2003**, *161*, 67–79.
- [9] R. Doshi, V. L. Richards, J. D. Carter, X. Wang, M. Krumpelt, *J. Electrochem. Soc.* **1999**, *146*, 1273–1278.
- [10] R. Maric, S. Ohara, T. Fukui, H. Yoshida, M. Nishimura, T. Inagaki, K. Miura, *J. Electrochem. Soc.* **1999**, *146*, 2006–2010.
- [11] J. Hassoun, B. Scrosati, *Adv. Mater.* **2010**, *22*, 5198–5201.
- [12] A. S. Best, M. Forsyth, D. R. MacFarlane, *Solid State Ionics* **2000**, *136*–*137*, 339–344.
- [13] Y. Inaguma, L. Q. Chen, M. Itoh, T. Nakamura, T. Uchida, H. Ikuta, M. Wakihara, *Solid State Commun.* **1993**, *86*, 689–693.
- [14] V. Thangadurai, S. Narayanan, D. Pinzarlu, *Chem. Soc. Rev.* **2014**, *43*, 4714–4727.
- [15] J. B. Goodenough, P. Singh, *J. Electrochem. Soc.* **2015**, *162*, A2387–A2392.
- [16] a) X. C. Lu, G. G. Xia, J. P. Lemmon, Z. G. Yang, *J. Power Sources* **2010**, *195*, 2431–2442; b) J. L. Sudworth, P. Barrow, W. Dong, B. Dunn, G. C. Farrington, J. O. Thomas, *MRS Bull.* **2000**, *25*, 22–26.
- [17] R. M. German, *Sintering Theory and Practice*, John Wiley & Sons, New York, **1996**, pp. 142–173.
- [18] a) D. O. Shin, K. Oh, K. M. Kim, K. Y. Park, B. Lee, Y. G. Lee, K. Kang, *Sci. Rep.* **2015**, *5*, 18053; b) C. W. Ban, G. M. Choi, *Solid State Ionics* **2001**, *140*, 285–292.
- [19] a) M. E. Badding, J. L. Brown, K. A. Jewell, A. V. Gagov, C. W. Tanner (Corning Incorporated), US-2014/0065513 A1, **2012**; b) N. B. Aetukuri, S. Kitajima, E. Jung, L. E. Thompson, K. Virwani, M. L. Reich, M. Kunze, M. Schneider, W. Schmidbauer, W. W. Wilcke, D. S. Bethune, J. C. Scott, R. D. Miller, H. C. Kim, *Adv. Energy Mater.* **2015**, *5*, 1500264.
- [20] a) G. Adachi, N. Imanaka, H. Aono, *Adv. Mater.* **1996**, *8*, 127–135; b) J. Plocharski, W. Wieczorek, *Solid State Ionics* **1988**, *28*–*30*, 979–982; c) D. R. MacFarlane, K. M. Nairn, P. J. Newman, M. Forsyth, *Electrochim. Acta* **1998**, *43*, 1333–1337; d) K. M. Nairn, A. S. Best, P. J. Newman, D. R. MacFarlane, M. Forsyth, *Solid State Ionics* **1999**, *121*, 115–119.
- [21] a) M. Cretin and P. Fabry, *J. Eur. Ceram. Soc.* **1999**, *19*, 2931–2940; b) C. W. Ban, G. M. Choi, *Solid State Ionics* **2001**, *140*, 285–292.
- [22] a) T. S. te Velde, G. W. M. T. van Helden, *Philips Tech. Rev.* **1968**, *29*, 238–242; T. S. te Velde, “Method of Manufacturing Electronic Devices, In Particular Semiconductor Devices,” U. S. Patent 3,796,782, Mar 12, 1974, assigned to U. S. Philips Corporation.
- [23] D. A. Woodcock, P. Lightfoot, *J. Mater. Chem.* **1999**, *9*, 2907–2911.
- [24] J. J. Cleveland, R. C. Bradt, *J. Am. Ceram. Soc.* **1978**, *61*, 478–481.

Manuscript received: February 24, 2020

Revised manuscript received: March 2, 2020

Version of record online: March 19, 2020